

Piezoelectric transducer design for simultaneous ultrasonic power transfer and backscatter communication

Ahmed Allam* , Karim Sabra and Alper Erturk 

G.W. Woodruff School of Mechanical Engineering, Georgia Institute of Technology, Atlanta, GA, United States of America

E-mail: a.allam@gatech.edu

Received 20 April 2022, revised 29 May 2022

Accepted for publication 22 June 2022

Published 6 July 2022



CrossMark

Abstract

Ultrasonic waves can transfer power and data to sensors and devices deployed to traditionally inaccessible locations, such as inside the human body or deep in the ocean, eliminating the need for battery replacement. In ultrasonic power and data transfer systems, a piezoelectric transducer converts incident ultrasonic waves to useful electric power while transmitting data by modulating its reflected signal through backscatter communication. Existing approaches rely on reflecting a portion of the incident power to communicate, reducing the harvested power. This work realizes uninterrupted power harvesting with simultaneous backscatter communication through frequency multiplexing. A piezoelectric transducer is first designed and tested experimentally for high sensitivity and high bandwidth operation through low-loss broadband acoustic and electrical impedance matching. The transducer achieved 70% bandwidth at 1 MHz with a 10 dB difference between reflecting and absorbing incident ultrasonic waves. A frequency multiplexing technique is then developed to separate power and data into different frequency bands achieving simultaneous operation. The technique extends the range and bandwidth of ultrasonically powered devices such as biomedical implants and ocean monitoring sensors.

Keywords: acoustic power transfer, piezoelectric transducers, impedance matching, backscatter communication

(Some figures may appear in colour only in the online journal)

1. Introduction

Ultra-low-power electronic circuits and sensors enable devices to be deployed in traditionally inaccessible locations such as inside the brain [1], in sealed metallic enclosures [2], or deep in the ocean [3, 4]. The limited accessibility in these environments for battery replacement and the need for long-distance transmission as well as deep-implants have motivated researchers to consider ultrasonic waves for transmitting both power and data to the device. Ultrasonic waves solve various challenges in different research domains from medicine

to defense industry, and the solutions developed for each field exhibit similarities.

Biomedical technology researchers use ultrasonic waves for powering and communicating with implanted medical devices [5] for health monitoring [6–11], enhancing tumor treatment [12, 13], neural recording [1, 14], and neural stimulation [15–21]. Ultrasonic power is utilized since the United States Food and Drug Administration limits the electromagnetic power transmitted through the human body to 0.1 mW mm^{-2} . In contrast, ultrasonic waves can have a power density as high as 7.2 mW mm^{-2} [22]. Ultrasonic waves also have a smaller wavelength than electromagnetic waves, allowing for smaller implants. Ultrasonic power delivery and communication is one of the

* Author to whom any correspondence should be addressed.

enabling technologies for concepts such as the body area network [23, 24].

Ultrasonic waves are also investigated for deep underwater communication solutions [25]. While optical and RF-based solutions exist, their operation is typically limited to short links due to the large attenuation of electromagnetic waves underwater [25, 26]. Underwater wireless ultrasonic sensor nodes are investigated for ocean monitoring and tracking climate change [27, 28], increasing underwater communication bandwidth [29], tracking marine life [30–32], and as markers for aiding the navigation of autonomous underwater vehicles [33]. Most of the devices developed in the underwater literature are battery-operated, limiting their lifespan given the difficulties in retrieving and replacing the batteries. However, recent efforts have investigated ultrasonic waves for both powering and communicating with underwater sensor nodes [3, 4, 34, 35].

Researchers have also investigated ultrasonic power and data transfer (UPDT) through metals [2, 36–42]. Since RF waves cannot penetrate thick metallic enclosures, mechanical waves remain the only power and data transfer approach. Sealed metallic enclosures equipped with UPDT systems protects sensitive electronics from electromagnetic interference, and provides complete weather protection.

All UPDT systems reviewed in the literature included a lead zirconate titanate (PZT) transmitter (TX) connected to an electrical power source. The power and data are transmitted to a piezoelectric receiver (RX) connected to either a sensor (for collecting data) or an actuator (for stimulating its environment). The data can flow from the transmitter to the receiver (downlink communication for sending excitation commands) [2, 15, 16, 18, 20, 43], from the receiver to the transmitter (uplink communication to transmit sensor data and device status) [1, 4, 6, 8, 10, 11, 14, 41, 42, 44–46], or in both directions either simultaneously (full-duplex) [40, 47] or in turns (half-duplex/time multiplexing) [21, 36, 48–51]. Downlink communication can be as simple as switching between turning the transmitter on and off, i.e. on-off keying [16] or using advanced modulation schemes such as orthogonal frequency division multiplexing (OFDM) for higher throughput [2].

Uplink communication has more restrictions than downlink since the power available to the wireless device is limited. While active approaches (exciting the transducer to send data) have been proposed for uplink communication, their realization usually involves toggling between storing enough power and transmitting the uplink data [4, 8]. Since no communication occurs while the wireless device is being charged, the uplink throughput is limited. It also requires a large capacitor or a battery to store the data, which might not be feasible in space-limited applications such as biomedical implants.

Ultrasonic backscatter is a passive uplink communication approach in which the reflected ultrasonic signal from RX is modulated to send the uplink data. In backscatter communication, the electrical impedance connected to the piezoelectric receiver is modulated, changing the receiver's

acoustic impedance and the amplitude of the reflected ultrasonic signal. By switching between absorbing and reflecting the ultrasonic waves, as shown in figure 1(a), uplink communication is established with minimal power from RX. Only a low-power transistor (with its driving circuit) provides uplink communication using backscatter reducing hardware complexity compared to active approaches. The majority of the surveyed literature incorporated backscattering in their UPDT designs [10, 34, 40, 48].

State-of-the-art UPDT systems reflect a portion of the incident ultrasonic power to establish backscatter communication limiting the amount of ultrasonic power they can absorb. As shown in figure 1(a), when the transistor is on, ultrasonic power flows to the energy harvesting circuit (rectification and voltage regulation) and is stored for the device operation. However, no power is harvested when the transistor is off, and most of the incident acoustic power is reflected. Ozeri and Shmilovitz [45] attempted to address this issue by introducing a slight change in the load connected to the transducer instead of completely shorting it. Still, their approach only compromised communication sensitivity and power harvesting.

This work realizes uninterrupted power harvesting with simultaneous backscatter communication through frequency multiplexing. A frequency band is dedicated to continuous power transfer and isolated from the data frequency bands. As shown in figure 1(b), the signal is split using a frequency splitter (also known as a diplexer in RF literature or frequency crossover in audio literature), and power is supplied continuously to an energy harvesting circuit uninterrupted by switching the data channel. However, in order to achieve frequency multiplexing, the piezoelectric receiver must have both high bandwidth and sensitivity which is achieved through careful broadband impedance matching of the piezoelectric transducer to both the acoustic and electric domains.

We first introduce a simplified analytical model for analyzing the reflection from a piezoelectric layer in section 2. Simultaneous acoustic and electric impedance matching of an air-backed piezoelectric transducer is then discussed in section 3. Several air-backed transducers are fabricated, and their performance is characterized in section 4 to evaluate the quality of the acoustic matching layers. Finally, the transducer is electrically matched for broadband data transfer and uninterrupted power delivery in section 5.

2. Modeling reflection from a piezoelectric layer

Consider a transducer made of a thin piezoelectric disc of thickness h_p and area A_p . The transducer is poled in the thickness direction with thin electrodes plated on each face. Figure 2 shows the transducer connected to an electric load with equivalent complex electrical impedance Z_e . The front face of the transducer is submerged underwater, and its back is in contact with a material with mechanical impedance Z_b . The impedance matrix (\mathbf{Z}) of the transducer relates the input forces on the front and back faces (F_1, F_2) and voltage

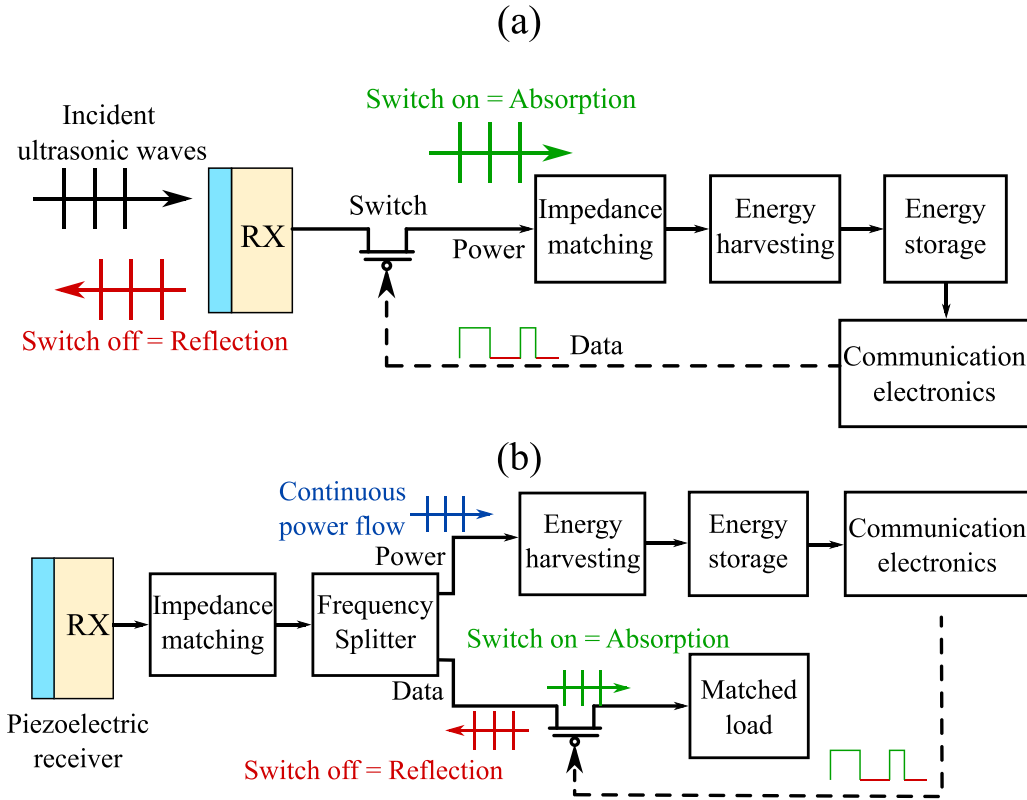


Figure 1. (a) Existing implementation of ultrasonic power and data transfer in literature. (b) Proposed system for simultaneous power and data transfer based on frequency multiplexing.

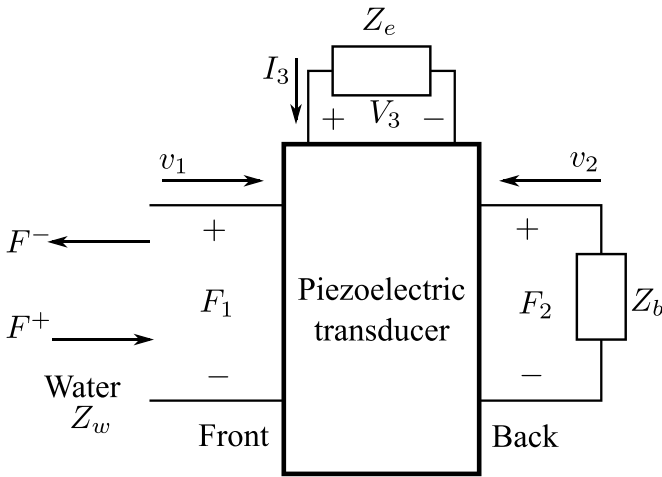


Figure 2. A schematic of a piezoelectric disc transducer represented as a three-port element connected to arbitrary electrical impedance Z_e and an arbitrary backing layer with mechanical impedance Z_b .

(V_3) to the velocities (v_1, v_2) and current (I_3). Z is given by [52]:

$$\begin{bmatrix} F_1 \\ F_2 \\ V_3 \end{bmatrix} = -j \underbrace{\begin{bmatrix} Z_p \cot(k_p h_p) & Z_p \csc(k_p h_p) & \frac{\bar{h}_{33}}{\omega} \\ Z_p \csc(k_p h_p) & Z_p \cot(k_p h_p) & \frac{\bar{h}_{33}}{\omega} \\ \frac{\bar{h}_{33}}{\omega} & \frac{\bar{h}_{33}}{\omega} & \frac{1}{\omega C_p} \end{bmatrix}}_{Z} \begin{bmatrix} v_1 \\ v_2 \\ I_3 \end{bmatrix},$$

where $Z_p = \rho_p c_p A_p$ is the mechanical impedance of the piezoelectric layer, ρ_p is the density, c_p is the longitudinal wave speed, $\bar{h}_{33} = e_{33}/\epsilon_{33}^s$ is known as the transmitting coefficient, e_{33} is the piezoelectric voltage constant, ϵ_{33}^s is the permittivity at constant strain, $k_p = \omega/c_p$ is the wavenumber in the piezoelectric layer, and $C_p = \epsilon_{33}^s A_p/h_p$ is the piezoelectric layer capacitance at constant strain (i.e. when mechanically clamped).

The electrical and backing impedance yield the equations:

$$F_2 = -v_2 Z_b \quad (2)$$

$$V_3 = -I_3 Z_e \quad (3)$$

which are substituted in equation (1) to find the input mechanical impedance of the transducer Z_{in} :

$$Z_{in} = \frac{F_1}{v_1} = Z_{11} - \frac{Z_{12}^2 - \frac{Z_{12}Z_{13}^2}{Z_e + Z_{33}}}{Z_b + Z_{11} - \frac{Z_{13}^2}{Z_e + Z_{33}}} - \frac{Z_{13}^2 - \frac{Z_{12}Z_{13}^2}{Z_b + Z_{11}}}{Z_e + Z_{33} - \frac{Z_{13}^2}{Z_b + Z_{11}}} \quad (4)$$

where Z_{mn} are the elements of the impedance matrix. The value of Z_{in} determines the amount of acoustic reflection from the transducer. Equation (4) shows that Z_{in} is a function of the transducer geometry and material, the backing layer impedance, and the electrical impedance. By changing the

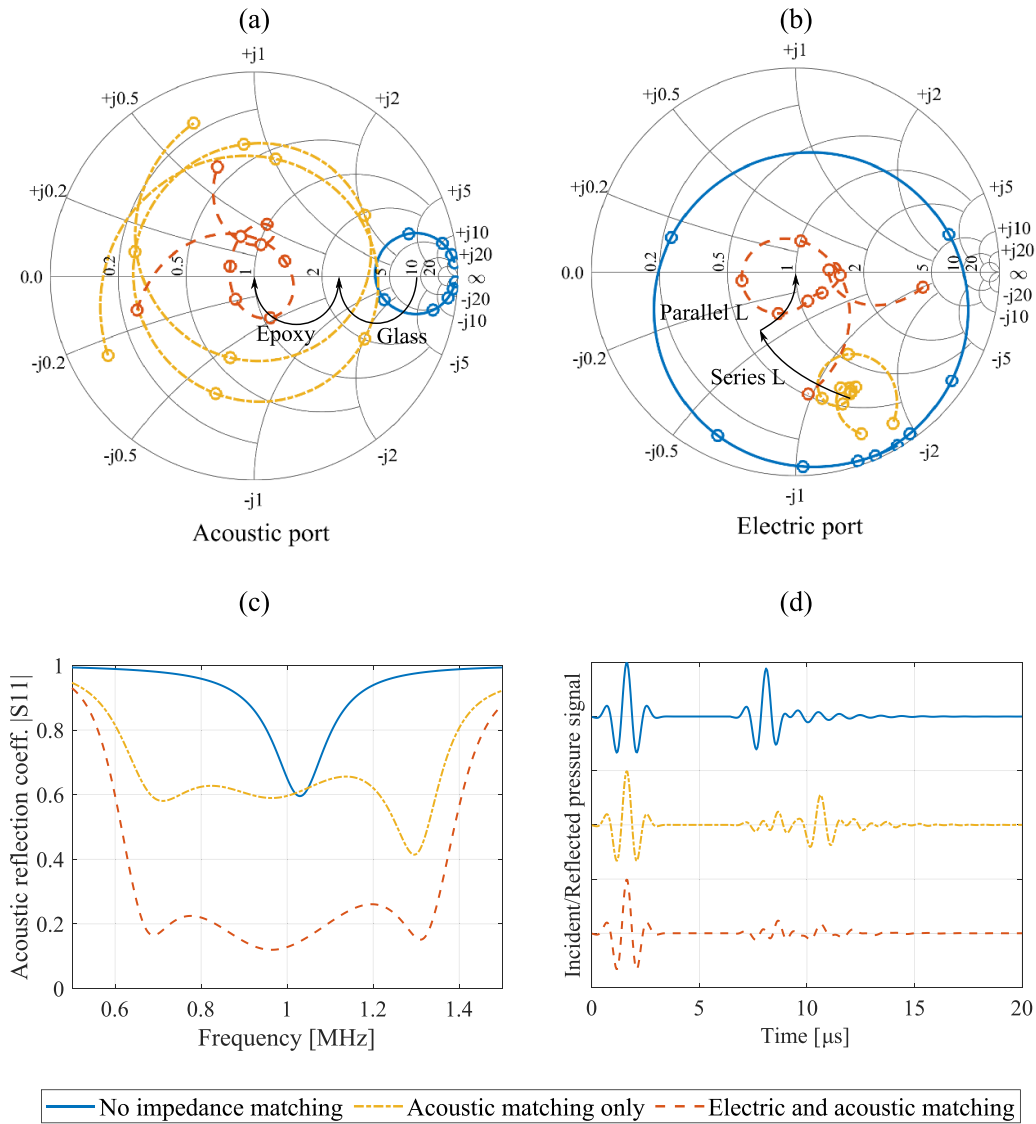


Figure 3. Smith charts of the analytical (a) acoustic and (b) electric reflection coefficients of the developed piezoelectric transducer showing the impedance matching steps. The amplitude of the acoustic reflection is shown for each step in (c). The incident and reflected acoustic pulses in the time domain are shown in (d).

electrical impedance connected to the transducer, its mechanical impedance changes enabling backscatter communication.

The amount of reflection is calculated using the complex reflection coefficient of the piezoelectric transducer (S_{11}) by assuming incident and reflected mechanical waves F^+ , F^- on the front face of the transducer, as shown in figure 2. The incident and reflected waves are related to the total force and velocity by:

$$\begin{aligned} F_1 &= F^+ + F^- \\ v_1 &= \frac{F^+ - F^-}{Z_w} \end{aligned} \quad (5)$$

where $Z_w = \bar{Z}_w A_p$ and \bar{Z}_w is the characteristic acoustic impedance of water in Rayleighs. The complex reflection coefficient (S_{11}) is defined as:

$$S_{11} = \frac{F^-}{F^+}. \quad (6)$$

By solving equations (4) and (5) together, the complex reflection coefficient of the transducer with respect to water is given by:

$$S_{11} = \frac{Z_w - Z_{in}}{Z_w + Z_{in}}. \quad (7)$$

This equation assumes that the piezoelectric layer is in direct contact with water. If acoustic matching layers are present, the transfer matrix method is used to calculate the reflection from the matched transducer [53].

The Smith chart is a useful tool for visualizing the complex reflection coefficient (S_{11}). Since the magnitude of the reflection coefficient cannot be greater than one, all its possible values are inside the unit circle, and thus the shape of the chart is circular as shown in figure 3. A reflection coefficient value close to the origin of the chart represents low reflection, and therefore a better match to a reference impedance. For acoustic ports, the reference impedance is the mechanical impedance

of the medium in which the transducer will operate, such as water, tissue, or metal. For electric ports, this reference impedance is commonly chosen to be 50Ω in RF circuits; however, it can be set to the impedance of any electric load that needs to be powered.

Impedance matching aims to minimize the reflection coefficient by adding electrical or mechanical elements that shifts the system's impedance towards the center of the plot. The horizontal line in the middle of the chart represents a purely resistive impedance, while the top and bottom halves represent inductive and capacitive impedance, respectively. Lines of constant resistance, reactance, conductance, and susceptance can be shown on the chart to guide the impedance matching efforts. All the values displayed on the chart are normalized to the chosen reference impedance. A more comprehensive discussion of the Smith chart can be found elsewhere in the existing literature [54].

3. Acoustic and electrical impedance matching of piezoelectric transducers

A 1 MHz piezoelectric disc transducer of thickness 2.1 mm and diameter 30 mm is selected to demonstrate simultaneous acoustic and electrical impedance matching. The transducer is made of a hard piezoelectric material (PZT-4) since it has a high piezoelectric coefficient and low damping to maximize coupling and minimize the power dissipated. The material properties of the piezoelectric layer are summarized in table 1.

The backing layer of common commercial transducers is usually made of a lossy material with impedance close to PZT which is well suited for imaging applications. This backing approach increases the transducer's bandwidth at the expense of lower sensitivity. Nearly half the input power to the transducer is lost to the backing layer in this configuration. To avoid power loss to in the transducer backing, air backing is used since it has a large impedance mismatch with PZT-4, which increases the efficiency and sensitivity of the transducer. Next, the transducer bandwidth is enhanced through simultaneous electrical and acoustic impedance matching.

Figure 3 shows the steps for enhancing the bandwidth and sensitivity of an air-backed transducer using electrical and acoustic impedance matching. The transducer is modeled using the transfer matrix method, and its impedance and reflection characteristics were simulated using MATLAB. First, the air-backed transducer without impedance matching is shown on the Smith chart (figures 3(a) and (b)) as solid blue lines. The electrical impedance of the bare transducer appears as a large circle which complicates electrical matching efforts since the impedance varies between a wide range of capacitive and inductive values depending on the frequency. The electrical impedance variation is reduced when the acoustic port is matched to water by shifting the acoustic impedance in figure 3(a) closer to the origin using quarter wavelength matching layers as commonly done in the literature [55].

In the literature, a single quarter wavelength matching layer is commonly used to match piezoelectric transducers to water. The material for a quarter wavelength matching layer needs to

Table 1. Material properties of PZT-4 used in the transducer 1D model.

Property	ρ_p	c_p	\bar{h}_{33}	C_{33}^D	C_p	Q_m	$\tan \delta$
Unit	kg m^{-3}	m s^{-1}	kV mm^{-1}	GPa	nF	—	%
Value	7500	4706	2727	166	1.98	500	0.4

have an acoustic impedance at the geometric mean of the two mediums that need to be matched, i.e. for matching a piezoelectric transducer to water:

$$Z_m = \sqrt{Z_p Z_w} \quad (8)$$

where $Z_m = 7 \text{ MRayl}$ is the acoustic impedance of the single matching layer. However, low-loss natural materials with an acoustic impedance close to 7 MRayl are rare, limiting the usefulness of single matching layers in high sensitivity/low loss applications such as UPDT [56]. Alternatively, two quarter wavelength layers can be used to enhance the piezoelectric transducer's bandwidth [56, 57]. The impedance of each matching layer is calculated from [58]:

$$Z_{m1} = Z_p^{2/3} Z_w^{1/3} \quad (9)$$

$$Z_{m2} = Z_p^{1/3} Z_w^{2/3} \quad (10)$$

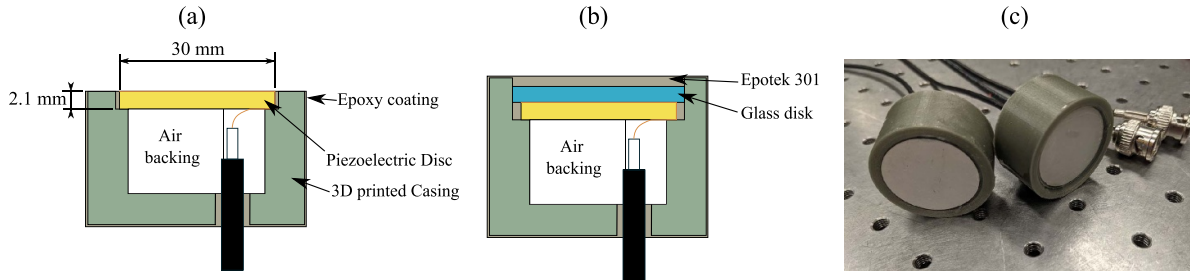
where Z_{m1} is the matching layer adjacent to the transducer, and Z_{m2} is adjacent to water. The acoustic impedance of quartz glass is around 12.1 MRayl which is very close to Z_{m1} value from equation (10). The value calculated for Z_{m2} is 4.3 MRayl , which lies in the neighborhood of metal-filled epoxies such as silver epoxy or tungsten-filled epoxy. These materials, however, are lossy and may reduce the sensitivity of the transducer. Pure epoxy (3 MRayl) has lower attenuation and is easy to cast and polish to exact thickness for fine-tuning the matching process, so it was used instead. Epotek-301 epoxy was selected since it is commonly used in the ultrasound literature because of its low viscosity, which allows it to be easily cast without trapping air bubbles.

The acoustic and electrical reflection coefficients for a two-layer matched transducer are shown as dot-dashed yellow lines in figure 3. The electrical impedance variation was reduced significantly after the acoustic impedance matching, as shown in figure 3(b). The electrical impedance is shifted to the center of the Smith chart to match the transducer electrically. A $6 \mu\text{H}$ series inductor and a $15 \mu\text{H}$ parallel inductor were used, as indicated in figure 3(b). Figure 3(c) shows that the matched transducer achieves a wide flat bandwidth close to 80% with a large sensitivity.

Figure 3(d) shows the acoustic reflection from the transducer in the time domain. A Gaussian pulse centered around 1 MHz with a bandwidth of 50% is incident on the transducer, and the reflected pulses are analyzed. The impedance-matched transducer converts most of the incident pulse into electrical energy, and a much smaller pulse is reflected compared to the bare transducer.

Table 2. Dimensions of the fabricated transducers.

Layer	Unit	U1	M1	M2	M3
PZT	mm	2.1	2.1	2.1	2.1
Epoxy	μm	—	10	10	10
Quartz glass	mm	—	1.6	1.6	1.56
Epotek 301	mm	—	0.4	0.5	0.6

**Figure 4.** (a) Schematic of an air-backed transducer without acoustic matching layers. (b) Construction of the two-layer acoustically matched transducer. (c) Fabricated transducers U1 and M1 before polishing.

4. Experimental verification

A set of transducers (M1–M3) were fabricated with two acoustic matching layers, as discussed in section 3. The epoxy layer was varied between 0.65 and 0.75 mm to obtain a transducer with the best possible match between the electrical and the acoustic domains. Additionally, an air-backed transducer without acoustic matching (U1) was fabricated to act as a baseline. The dimensions of the fabricated transducers are summarized in table 2.

4.1. Transducer fabrication

The transducers casings were 3D printed using an Ultimaker 3 printer. The casings shown in figure 4 were designed to provide air backing to the transducers by only supporting the piezoelectric layers from the edge. The unmatched transducer was fabricated by first soldering a coaxial cable to the back of the piezoelectric transducer (Steminc SMD30T21F1000R). The transducer was mounted in the casing, as shown in figure 4(a), and the gaps were sealed using 3M DP100 epoxy.

The matched transducers (figure 4(b)) were fabricated by first bonding a $1.25'' \times 0.0625''$ fused quartz glass disc, supplied by TGP Inc. ($\rho_1 = 2200 \text{ kg m}^{-3}$, $c_1 = 5500 \text{ m s}^{-1}$, $Z_1 = 12.1 \text{ MRayl}$, $\alpha_1 = 5 \text{ dB m}^{-1} \text{ MHz}^{-1}$) [59], to the front face of the piezoelectric transducer through a vacuum bonding process. The thickness of the glass disk $1/16''$ (1.56 mm) is slightly larger than the quarter wavelength thickness at 1 MHz (1.43 mm). A coaxial cable was soldered to the piezoelectric disc, and the transducer/glass assembly was mounted inside the casing. The casing was designed so that the remaining height acts as a mold for the epoxy matching layer. The transducer was sealed and coated using Epotek 301 epoxy ($\rho_2 = 1090 \text{ kg m}^{-3}$, $c_2 = 2640 \text{ m s}^{-1}$, $Z_2 = 2.85 \text{ MRayl}$, $\alpha_2 = 250 \text{ dB m}^{-1} \text{ MHz}^{-1}$) [59], and a heat gun was used to ensure that no air bubbles remained trapped in the epoxy layer before leaving it to cure for 24 h. The cured layer was then

Table 3. Experimentally identified modified PZT-4 material properties from electrical impedance data in air.

Property	ρ_p	c_p	\bar{h}_{33}	C_{33}^D	C_p	Q_m	$\tan \delta$
Unit	kg m^{-3}	m s^{-1}	kV mm^{-1}	GPa	nF	—	%
Value	7900	4714	2313	175	2.4	500	0.4

sanded down till it was flush with the front of the casing using 200 grit sandpaper followed by 400 grit, then 600 grit. The fabricated transducers are shown in figure 4(c).

4.2. Measuring the electrical impedance of the transducers

An Agilent 33250A signal generator and a Tektronix TDS5034B oscilloscope were used to measure the electrical impedance of the fabricated transducers experimentally. The signal generator was connected to the tested transducer and then programmed to apply a voltage chirp signal that swept from 100 kHz up to 2 MHz. The applied voltage and the current flowing to the transducer were measured simultaneously using a 150 MHz voltage probe and a current probe (Tektronix P6022). The voltage and current signals were then converted to the frequency domain and used to calculate the input electrical impedance of the transducer.

The electrical impedance of an unmatched transducer in air was first used to estimate the exact piezoelectric material properties using the procedure described in reference [60]. The experimentally measured piezoelectric properties are summarized in table 3.

The transducers' electrical impedance was measured underwater in a $30'' \times 20'' \times 15''$ water tank. The experimental electric impedance of the different transducers is compared to the analytical predictions in figure 5. The experimental results agree well with the analytical predictions with a slight deviation caused by the uncertainties in the material properties and geometry of the different layers. The acoustic

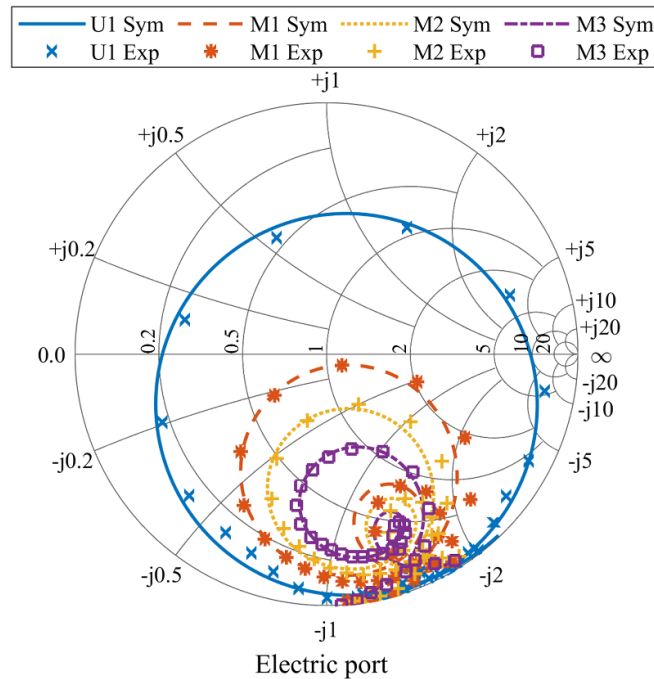


Figure 5. Analytical (lines) and experimental (markers) electric impedance for three matched transducers (M1–M3) with different epoxy layer thickness as summarized in table 2. The impedance of a transducer without acoustic matching (U1) is shown for reference.

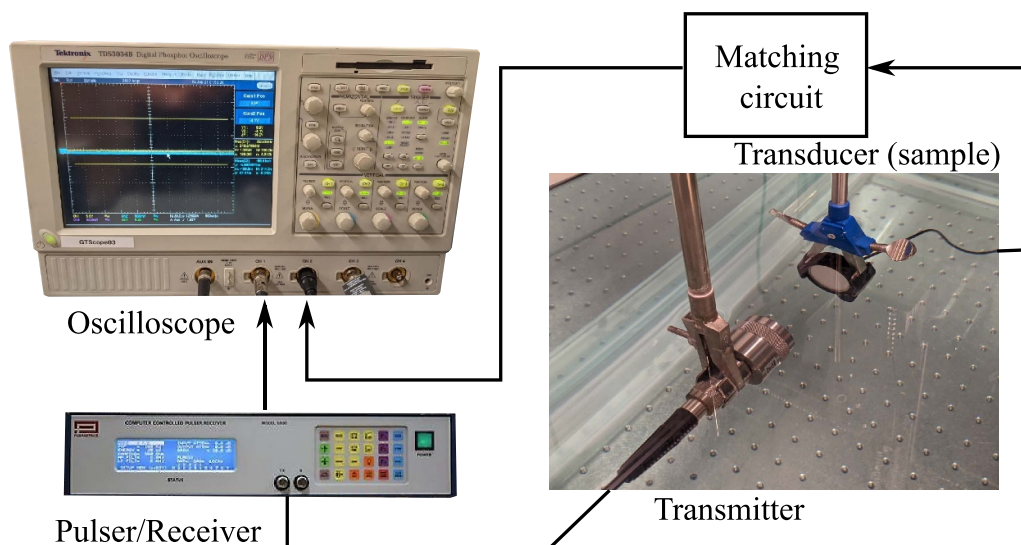


Figure 6. Experimental setup for measuring the acoustic reflection coefficient of the fabricated transducers.

matching of the transducer was sensitive to the thickness of the glass and epoxy layers, as shown by circle size difference between transducers M1–M3. A better acoustic impedance match can be achieved by fine-tuning the glass and epoxy layers geometry as predicted in figure 3. Transducer M3 showed the best acoustic matching (smallest circle in the Smith chart), so it was selected for subsequent electrical impedance matching.

4.3. Setup for measuring the acoustic reflection coefficient

The acoustic reflection coefficient of the fabricated transducers was measured using the setup shown in figure 6. A

Panametrics 5800 pulser/receiver was used to excite a broadband Olympus V394 source transducer. The reflected echo signal at the source transducer was filtered and amplified by the pulser and routed to an oscilloscope for display and recording. The pulser was set to excite the transducer with a $12.5 \mu\text{J}$ pulse with a repetition rate of 500 Hz. The echo signal was filtered with a 100 kHz–10 MHz bandpass filter to reduce the noise then amplified with a 20 dB gain.

The acoustic reflection coefficient of the samples was calibrated using the echo from normal incidence on a stainless-steel 304 cylinder of 26.4 mm thickness and 101 mm diameter. Normal incidence was verified by rotating the calibration cylinder until the maximum echo amplitude was achieved. The

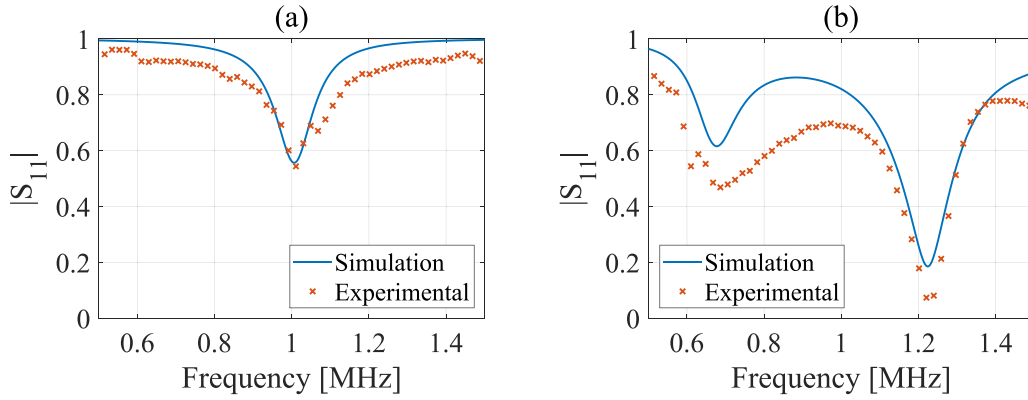


Figure 7. Experimental versus analytical acoustic reflection coefficient for (a) the transducer without acoustic matching (U1), and (b) the two-layer acoustically matched transducer (M3).

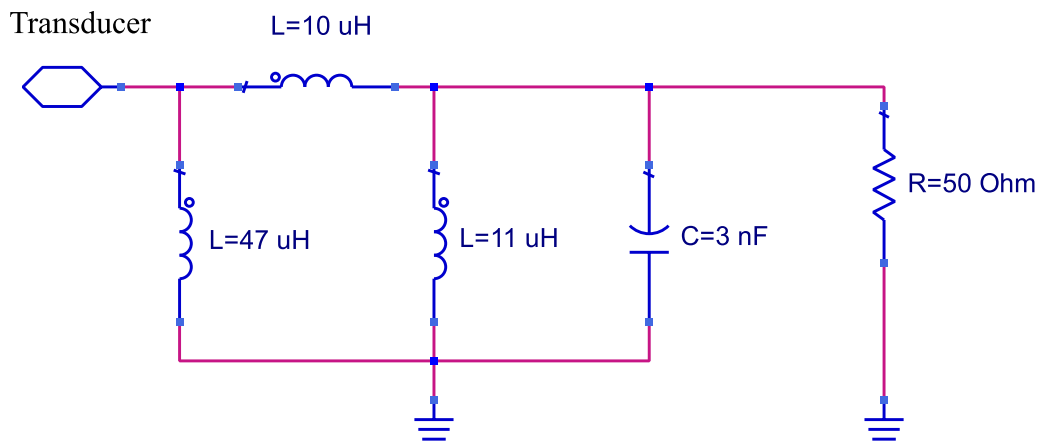


Figure 8. Electrical circuit used to achieve broadband electrical impedance matching for the acoustically matched transducer (M3).

first echo from the calibration cylinder was windowed and then converted to the frequency domain. The acoustic reflection coefficient from the sample was then calculated using the relation:

$$S_{11} = R_{st} \frac{A_{\text{sample}}}{A_{\text{calib}}} \quad (11)$$

where A_{sample} is the reflected signal from the sample, A_{calib} is the reflected signal from the stainless-steel cylinder, and R_{st} is the reflection coefficient of a water–steel interface calculated from:

$$R_{st} = \frac{Z_{st} - Z_w}{Z_{st} + Z_w} \quad (12)$$

where $Z_{st} = 46.57 \text{ MRayl}$ is the acoustic impedance of stainless steel.

The experimental acoustic reflection coefficients for the unmatched and matched transducers (U1 and M3) are compared to the analytical models in figure 7. The reflection coefficient is measured and simulated with respect to a 50Ω output for both samples, i.e. no electrical matching was done for this measurement. For both samples, the amplitude of the experimental reflection coefficient is lower than the simulations for all frequencies. This shift is caused by unmodeled losses due to diffraction and misalignment between the transducers.

The two-layer acoustically matched transducer M3 was first electrically matched to achieve maximum bandwidth while connected to a 50Ω electric load. The four-element electrical matching network shown in figure 8 was designed and optimized using the impedance matching tool in Keysight Advanced Design System software. The random optimization algorithm built into the software was used to minimize S_{22} for the frequency bandwidth between 0.5 MHz and 1.5 MHz. The four-element circuit was used instead of the two-element circuit proposed in section 3 due to the imperfections in the acoustic matching caused by the geometrical and material uncertainty.

The experimental acoustic reflection from the transducer with the matching circuit is compared to open circuit termination in figure 9. The matched transducer achieved up to 70% bandwidth centered around 900 kHz with a factor of 3 change in amplitude (10 dB) between the open circuit and matched states, as shown in figure 9(a). Considering the modulation of the echo signal shown in figure 9(b), at least 200 kbps of data can be transmitted using this setup with simple amplitude shift keying modulation. Higher data rates are possible with advanced modulation techniques such as OFDM. It should be noted that the echo signal in figure 9(b) is different from that estimated analytically in figure 3(d) for two reasons. First, the signal plotted in figure 9(b) is for the voltage signal captured

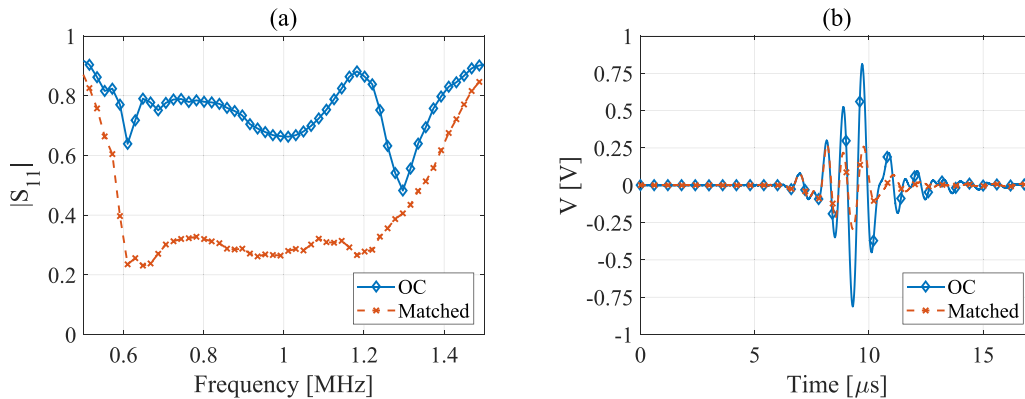


Figure 9. (a) Experimental acoustic reflection coefficient for an electrically and acoustically matched transducer. Broadband electrical matching is shown using the circuit in figure 8 versus when the transducer was open circuit. (b) Time waveform showing the modulation of the reflected pulse by varying electrical circuit connected to the transducer.

by the transmitter not the actual reflected pressure signal, i.e. the signal is multiplied by the two-way transfer function of the transmitter. Second, the impedance matching in figure 3 is different from that implemented experimentally due to the uncertainties in the acoustic matching.

5. Impedance matching for simultaneous power and data transfer

The matched transducer can be designed to receive power while transmitting data simultaneously by dividing its wide bandwidth between a narrowband power channel and a broadband data channel. This frequency multiplexing is realized using the circuit shown in figure 10. It is a frequency splitter designed to direct incident data signals with frequencies between 600 kHz and 900 kHz to a dummy communication load while directing the power signal (sent continuously at 1.3 MHz) to a power harvesting circuit. The splitter is realized using a series LC circuit as a narrow bandpass filter for the power signal. A second parallel LC circuit is used as a bandstop filter to pass all frequencies to a communication load except for the power frequency (1.3 MHz). The bandwidth of the bandstop filter is improved by adding a parallel capacitor for matching to the 50 Ω load. By switching the data branch on and off, the incident signal at data frequencies is modulated while the power signal is continuously fed to an energy harvesting circuit for powering the wireless device.

The circuit in figure 10(b) was implemented on a breadboard, and the experimental acoustic reflection coefficient was measured as shown in figure 11(a). The communication branch is switched to transmit backscatter communication signal in the frequency range between 600 kHz and 900 kHz. The power branch at 1.3 MHz is not affected by the communication signal and almost all the power incident on the transducer at this frequency is absorbed.

The normalized spectrum of the voltage signals received at the different branches of the system are shown in figure 11(b). The communication branch load absorbs the incident power in the data channel frequency range (600–900 kHz) while

rejecting the power signal above 1 MHz. The time signal for the echo received by the transmitter filtered in the data channel bandwidth between 600 kHz and 900 kHz is shown in figure 11(c). The difference between the amplitude of the two communication states is more than the double (6 dB), demonstrating high sensitivity.

The circuit shown in figure 11(b) was constructed using the fewest number of nominal inductor and capacitor values. The upper bound of the data bandwidth is limited by a guard band between the power and data channels that prevents power from leaking to the data band. The data bandwidth can be enhanced further using a higher order matching filter with more elements which allows for a narrower buffer zone. The power branch absorbs power most efficiently around the target frequency of 1.3 MHz, as indicated by the low reflection coefficient in figure 11(a). The sensitivity of the power branch is higher than the data branch due to its narrowband nature.

Several modifications to the electrical matching circuit are possible depending on the target application. For example, (a) the reliability of the power transfer can be improved by increasing its bandwidth while sacrificing some sensitivity and efficiency using a higher order filtering topology. (b) The data and power frequency channels can be swapped to allow for power transfer at lower frequencies (around 700 kHz) by modifying the filters' target frequencies. The power transmission frequency can be chosen to maximize the efficiency depending on the distance between the transmitter and the receiver, i.e. whether the system is limited by divergence losses (wave spreading) or attenuation. The matching filters used can be tweaked for allocating the power and data bands within the transducer bandwidth limited by the quality of the acoustic impedance matching. (c) The current implementation focused on the fundamental frequency of the piezoelectric transducer as a proof of concept; however, a larger bandwidth is available if the frequencies surrounding the odd harmonics of the piezoelectric transducer are considered. Finally, (d) the power received at the data channel when it is absorbing incident power (transmitting a zero by not reflecting the incident acoustic power) may also be routed to the energy harvesting circuit to increase the power harvested by the system.

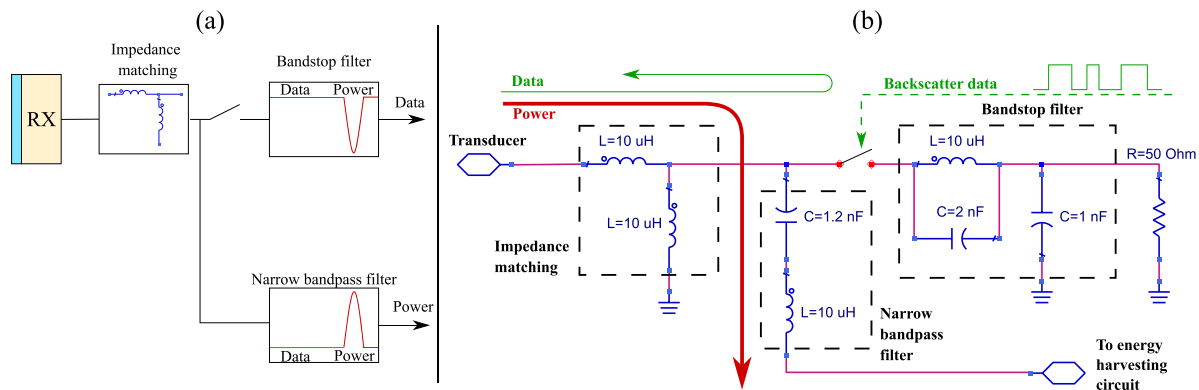


Figure 10. (a) Schematic and (b) implementation of an electrical circuit for simultaneous ultrasonic power and data transfer. The circuit routes incident power and data signals to two separate electrical branches allowing for uninterrupted power flow to an energy harvesting circuit while transmitting backscatter data.

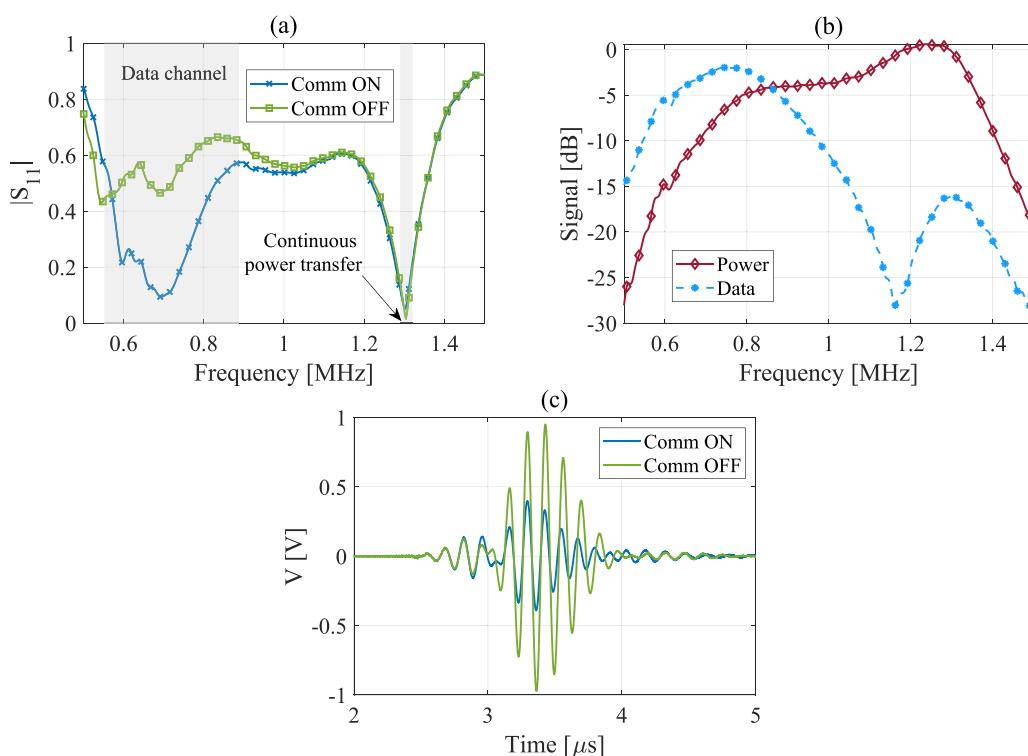


Figure 11. (a) Experimental acoustic reflection coefficient for a transducer connected to the simultaneous power and data transfer circuit shown in figure 8. (b) The spectrum of the signal received by the power branch of the circuit versus that received by the data branch for an incident ultrasonic pulse. (c) Filtered echo signal showing the data bandwidth between 600 kHz and 800 kHz.

6. Conclusions

A piezoelectric transducer was designed for maximum operating bandwidth while maintaining a high sensitivity. The transducer was matched acoustically using two quarter-wavelength layers and electrically using a four-element wideband matching circuit. Experimental characterization of the transducer verified a 600 kHz (70%) bandwidth with a 10 dB difference between connecting the matching circuit and keeping the transducer open, allowing for reliable backscatter communication with high data rates.

A technique for simultaneous underwater power and data transfer using a single transducer was developed and

experimentally validated. The power and data signals were multiplexed to ensure uninterrupted power transmission to an underwater wireless sensor maintaining backscatter communication with large data bandwidth. A high sensitivity data bandwidth of 300 kHz was obtained while achieving uninterrupted power transfer with minimum reflection. A simultaneous UPDT system prototype is currently being developed to characterize the efficiency, delivered power, range, data throughput, and error rate using this technique. The developed technique has applications in biomedical implants, ocean monitoring and navigation, and through-metal ultrasonic transfer for shielded devices and enclosures.

Data availability statement

All data that support the findings of this study are included within the article (and any supplementary files).

Acknowledgment

The authors acknowledge support from U.S. National Science Foundation CMMI Grant No. 1727951.

ORCID iDs

Ahmed Allam  <https://orcid.org/0000-0001-7571-9608>

Alper Erturk  <https://orcid.org/0000-0003-0110-5376>

References

- [1] Seo D, Neely R M, Shen K, Singhal U, Alon E, Rabaey J M, Carmena J M and Maharbiz M M 2016 Wireless recording in the peripheral nervous system with ultrasonic neural dust *Neuron* **91** 529–39
- [2] Lawry T J, Wilt K R, Ashdown J D, Scarton H A and Saulnier G J 2013 A high-performance ultrasonic system for the simultaneous transmission of data and power through solid metal barriers *IEEE Trans. Ultrason. Ferroelectr. Freq. Control* **60** 194–203
- [3] Jang J and Adib F 2019 Underwater backscatter networking *SIGCOMM '19: Proc. ACM Special Interest Group on Data Communication* (Beijing: ACM) pp 187–99
- [4] Guida R, Demirors E, Dave N and Melodia T 2020 Underwater ultrasonic wireless power transfer: a battery-less platform for the internet of underwater things *IEEE Trans. Mob. Comput.* **21** 1861–73
- [5] Basaeri H, Christensen D B and Roundy S 2016 A review of acoustic power transfer for bio-medical implants *Smart Mater. Struct.* **25** 123001
- [6] Mazzilli F, Peisino M, Mitouassiou R, Cotté B, Thoppay P, Lafon C, Favre P, Meurville E and Dehollain C 2010 *In-vitro* platform for study ultrasound as source for wireless energy transfer and communication for implanted medical devices *2010 Annual Int. Conf. of the IEEE Engineering in Medicine and Biology* pp 3751–4
- [7] Mazzilli F, Lafon C and Catherine Dehollain A 2014 10.5 cm Ultrasound link for deep implanted medical devices *IEEE Trans. Biomed. Circuits Syst.* **8** 738–50
- [8] Weber M J, Yoshihara Y, Sawaby A, Charthad J, Chang T C and Arbabian A 2018 A miniaturized single-transducer implantable pressure sensor with time-multiplexed ultrasonic data and power links *IEEE J. Solid-State Circuits* **53** 1089–101
- [9] Alam M, Shuai Li, Ahmed R U, Yam Y M, Thakur S, Wang X-Y, Tang D, Serena N and Zheng Y-P 2019 Development of a battery-free ultrasonically powered functional electrical stimulator for movement restoration after paralyzing spinal cord injury *J. NeuroEng. Rehabil.* **16** 36
- [10] Shi C, Andino-Pavlovsky V, Lee S A, Costa T, Elloian J, Konofagou E E and Shepard K L 2021 Application of a sub-0.1 mm³ implantable mote for *in vivo* real-time wireless temperature sensing *Sci. Adv.* **7** eabf6312
- [11] Gil B, Anastasova S and Yang G Z 2021 Low-powered implantable devices activated by ultrasonic energy transfer for physiological monitoring in soft tissue via functionalized electrochemical electrodes *Biosens. Bioelectron.* **182** 113175
- [12] Maleki T, Cao N, Song S H, Kao C, Song-Chu K and Ziaie B 2011 An ultrasonically powered implantable micro-oxygen generator (IMOG) *IEEE Trans. Biomed. Eng.* **58** 3104–11
- [13] Kim A, Zhou J, Samaddar S, Song S H, Elzey B D, Thompson D H and Ziaie B 2019 An implantable ultrasonically-powered micro-light-source (μ Light) for photodynamic therapy *Sci. Rep.* **9** 1395
- [14] Piech D K, Kay J E, Boser B E and Maharbiz M M 2017 Rodent wearable ultrasound system for wireless neural recording *2017 39th Annual Int. Conf. of the IEEE Engineering in Medicine and Biology Society (EMBC)* pp 221–5
- [15] Tsai J-Y, Huang K-H, Wang J-R, Liu S-I and Li P-C 2011 Ultrasonic wireless power and data communication for neural stimulation *2011 IEEE Int. Ultrasonics Symp.* pp 1052–5
- [16] Luo Y-S, Wang J-R, Huang W-J, Tsai J-Y, Liao Y-F, Tseng W-T, Yen C-T, Pai-Chi Li and Liu S-I 2013 Ultrasonic power/data telemetry and neural stimulator with OOK-PM signaling *IEEE Trans. Circuits Syst. II* **60** 827–31
- [17] Charthad J, Weber M J, Chang T C and Arbabian A 2015 A mm-sized implantable medical device (IMD) with ultrasonic power transfer and a hybrid bi-directional data link *IEEE J. Solid-State Circuits* **50** 1741–53
- [18] Charthad J, Chang T C, Liu Z, Sawaby A, Weber M J, Baker S, Gore F, Felt S A and Arbabian A 2018 A mm-sized wireless implantable device for electrical stimulation of peripheral nerves *IEEE Trans. Biomed. Circuits Syst.* **12** 257–70
- [19] Lee B, Koripalli M K, Jia Y, Acosta J, Sendi M S E, Choi Y and Ghovanloo M 2018 An implantable peripheral nerve recording and stimulation system for experiments on freely moving animal subjects *Sci. Rep.* **8** 6115
- [20] Tacchetti L, Serdijn W A and Giagka V 2018 An ultrasonically powered and controlled ultra-high-frequency biphasic electrical neurostimulator *2018 IEEE Biomedical Circuits and Systems Conf. (BioCAS)* pp 1–4
- [21] Piech D K, Johnson B C, Shen K, Ghanbari M M, Li K Y, Neely R M, Kay J E, Carmena J M, Maharbiz M M, Muller R 2020 A wireless millimetre-scale implantable neural stimulator with ultrasonically powered bidirectional communication *Nat. Biomed. Eng.* **4** 207–22
- [22] FDA 2019 Marketing clearance of diagnostic ultrasound systems and transducers *Technical Report* FDA-2017-D-5372 (Federal Drug & Food Administration)
- [23] Seyedi M, Kibret B, Lai D T H and Faulkner M 2013 A survey on intrabody communications for body area network applications *IEEE Trans. Biomed. Eng.* **60** 2067–79
- [24] Jaafar B, Luo J, Firfilionis D, Soltan A, Neasham J and Degenaar P 2020 Ultrasound intra body multi node communication system for bioelectronic medicine *Sensors* **20** 31
- [25] Heidemann J, Stojanovic M and Zorzi M 2012 Underwater sensor networks: applications, advances and challenges *Phil. Trans. R. Soc. A* **370** 158–75
- [26] Lanbo L, Shengli Z and Jun-Hong C 2008 Prospects and problems of wireless communication for underwater sensor networks *Wirel. Commun. Mob. Comput.* **8** 977–94
- [27] Lloret J 2013 Underwater sensor nodes and networks *Sensors* **13** 11782–96
- [28] Pearlman J, Jirka S, del Rio J, Delory E, Frommhold L, Martinez S and O'Reilly T 2016 Oceans of Tomorrow sensor interoperability for *in-situ* ocean monitoring *OCEANS 2016 MTS/IEEE Monterey* pp 1–8
- [29] Stojanovic M 2007 On the relationship between capacity and distance in an underwater acoustic communication channel *ACM SIGMOBILE Mob. Comput. Commun. Rev.* **11** 34–43

- [30] Lowe C G, Holland K N and Wolcott T G 1998 A new acoustic tailbeat transmitter for fishes *Fisheries Res.* **36** 275–83
- [31] Fore M, Alfredsen J A and Gronningsater A 2011 Development of two telemetry-based systems for monitoring the feeding behaviour of Atlantic salmon (*Salmo salar* L.) in aquaculture sea-cages *Comput. Electron. Agric.* **76** 240–51
- [32] Huidong Li, Tian C, Jun L, Myjak M J, Martinez J J, Brown R S and Deng Z D 2016 An energy harvesting underwater acoustic transmitter for aquatic animals *Sci. Rep.* **6** 33804
- [33] Paull L, Saeedi S, Seto M and Howard Li 2014 AUV navigation and localization: a review *IEEE J. Ocean. Eng.* **39** 131–49
- [34] Ghaffarivardavagh R, Afzal S S, Rodriguez O and Adib F 2020 Ultra-wideband underwater backscatter via piezoelectric metamaterials *Proc. Annual Conf. ACM Special Interest Group on Data Communication on the Applications, Technologies, Architectures and Protocols for Computer Communication, SIGCOMM '20* (New York: Association for Computing Machinery) pp 722–34
- [35] Guida R, Demirors E, Dave N, Rodowicz J and Melodia T August 2018 An acoustically powered battery-less internet of underwater things platform *2018 Fourth Underwater Communications and Networking Conf. (UComms)* pp 1–5
- [36] Shoudy D A 2007 An ultrasonic through-wall communication system with power harvesting *2007 IEEE Ultrasonics Symp. Proc.* pp 1848–53
- [37] Kluge M, Schalk T B, J and Otterpohl T 2008 Remote acoustic powering and data transmission for sensors inside of conductive envelopes *2008 IEEE Sensors* pp 41–44
- [38] Graham D J, Neasham J A and Sharif B S 2011 Investigation of methods for data communication and power delivery through metals *IEEE Trans. Ind. Electron.* **58** 4972–80
- [39] Lawry T J, Saulnier G J, Ashdown J D, Wilt K R, Scarton H A, Pascarelle S and Pinezich J D 2011 Penetration-free system for transmission of data and power through solid metal barriers *2011 - MILCOM 2011 Military Communications Conf.* pp 389–95
- [40] Jonathan D et al 2013 A full-duplex ultrasonic through-wall communication and power delivery system *IEEE Trans. Ultrason. Ferroelectr. Freq. Control* **60** 587–95
- [41] Farm-Guoo Tseng V, Bedair S S and Lazarus N 2018 Acoustic power transfer and communication with a wireless sensor embedded within metal *IEEE Sens. J.* **18** 5550–8
- [42] Takahashi V L, Kubrusly A C, Braga A M B, Quintero S M M, Figueiredo Savio W O and Domingues A B 2019 Ultrasonic power and data transfer through multiple curved layers applied to pipe instrumentation *Sensors* **19** 4074
- [43] Tang X, Sameer M and Mandal S 2018 Acoustic wireless power and data telemetry for structural health monitoring *2018 IEEE Sensors* pp 1–4
- [44] Roa-Prada S, Scarton H A, Saulnier G J, Shoudy D A, Ashdown J D, Das P K and Gavens A J 2013 An ultrasonic through-wall communication (UTWC) system model *J. Vib. Acoust.* **135** 011004
- [45] Ozeri S and Shmilovitz D 2014 Simultaneous backward data transmission and power harvesting in an ultrasonic transcutaneous energy transfer link employing acoustically dependent electric impedance modulation *Ultrasonics* **54** 1929–37
- [46] Rosa B M G and Yang G Z 2020 Towards integration of ultrasonic-powered implantable devices for physiological monitoring, stimulation and imaging in soft tissues using a handheld scanning probe *IEEE Sens. J.* **21** 14099–109
- [47] Suzuki S-nosuke, Kimura S, Katane T, Saotome H, Saito O and Kobayashi K 2002 Power and interactive information transmission to implanted medical device using ultrasonic *Jpn. J. Appl. Phys.* **41** 3600
- [48] Kawanabe H, Katane T, Saotome H, Saito O and Kobayashi K 2001 Power and information transmission to implanted medical device using ultrasonic *Jpn. J. Appl. Phys.* **40** 3865
- [49] Saulnier G J, Scarton H A, Gavens A J, Shoudy D A, Murphy T L, Wetzel M, Bard S, Roa-Prada S and Das P 2006 P1G-4 through-wall communication of low-rate digital data using ultrasound *2006 IEEE Ultrasonics Symp.* pp 1385–9
- [50] Kluge M, Sabater J, Josef Schalk L V Ngo H S and Schmid U 2007 Wireless sensing of physical parameters inside hermetically enclosed conductive envelopes *ASME 2007 Int. Design Engineering Technical Conferences and Computers and Information in Engineering Conf.* (American Society of Mechanical Engineers Digital Collection) pp 353–9
- [51] Johnson B C, Shen K, David Piech M, Ghanbari M, Li K Y, Neely R, Carmena J M, Maharbiz M M and Muller R 2018 StimDust: a 6.5 mm³, wireless ultrasonic peripheral nerve stimulator with 82% peak chip efficiency *2018 IEEE Custom Integrated Circuits Conf. (CICC)* pp 1–4
- [52] Kino G S 1987 *Acoustic Waves: Devices, Imaging and Analog Signal Processing* (Englewood Cliffs, NJ: Prentice Hall)
- [53] Lawry T J, Wilt K R, Scarton H A and Saulnier G J 2012 Analytical modeling of a sandwiched plate piezoelectric transformer-based acoustic-electric transmission channel *IEEE Trans. Ultrason. Ferroelectr. Freq. Control* **59** 2476–86
- [54] Poole C and Darwazeh I 2016 *Microwave Active Circuit Analysis and Design* (Oxford: Academic)
- [55] Rathod V T 2020 A review of acoustic impedance matching techniques for piezoelectric sensors and transducers *Sensors* **20** 4051
- [56] Bakhtiari-Nejad M, Hajj M R and Shahab S 2020 Dynamics of acoustic impedance matching layers in contactless ultrasonic power transfer systems *Smart Mater. Struct.* **29** 035037
- [57] Goll J H and Auld B A 1975 Multilayer impedance matching schemes for broadbanding of water loaded piezoelectric transducers and high Q electric resonators *IEEE Trans. Sonics Ultrason.* **22** 52–53
- [58] Alvarez-Arenas T E G 2004 Acoustic impedance matching of piezoelectric transducers to the air *IEEE Trans. Ultrason. Ferroelectr. Freq. Control* **51** 624–33
- [59] Selfridge A R 1985 Approximate material properties in isotropic materials *IEEE Trans. Sonics Ultrason.* **32** 381–94
- [60] Sherman C H and Butler J L 2007 *Transducers and Arrays for Underwater Sound* (New York: Springer)